ACS Catalysis

Research Article

pubs.acs.org/acscatalysis

High-Performance Oxygen Redox Catalysis with Multifunctional Cobalt Oxide Nanochains: Morphology-Dependent Activity

Prashanth W. Menezes,[†] Arindam Indra,[†] Diego González-Flores,[‡] Nastaran Ranjbar Sahraie,[§] Ivelina Zaharieva,[‡] Michael Schwarze,[†] Peter Strasser,*[,§,#] Holger Dau,*[,‡] and Matthias Driess*[,†]

[†]Department of Chemistry: Metalorganics and Inorganic Materials, Technische Universität Berlin, Straße des 17 Juni 135, Sekr. C2, 10623 Berlin, Germany

[‡]Fachbereich Physik, Freie Universität Berlin, Arnimallee 14, 14195 Berlin, Germany

[§]Department of Chemistry, The Electrochemical Energy, Catalysis, and Materials Science Group, Technische Universität Berlin, Straße des 17 Juni 124, Sekr. TC3, 10623 Berlin, Germany

[#]Ertl Center for Electrochemistry and Catalysis, Gwangju Institute of Science and Technology, Gwangju 500-712, South Korea

Supporting Information

ABSTRACT: Future advances in renewable and sustainable energy require advanced materials based on earth-abundant elements with multifunctional properties. The design and the development of cost-effective, robust, and high-performance catalysts that can convert oxygen to water, and vice versa, is a major challenge in energy conversion and storage technology. Here we report cobalt oxide nanochains as multifunctional catalysts for the electrochemical oxygen evolution reaction (OER) at both alkaline and neutral pH, oxidant-driven, photochemical water oxidation in various pH, and the electrochemical oxygen reduction reaction (ORR) in alkaline medium. The cobalt oxide nanochains are easily accessible on a multigram scale by low-temperature degradation of a cobalt oxalate precursor. What sets this study apart from earlier ones is its synoptical perspective of reversible oxygen redox catalysis in different chemical and electrochemical environments.

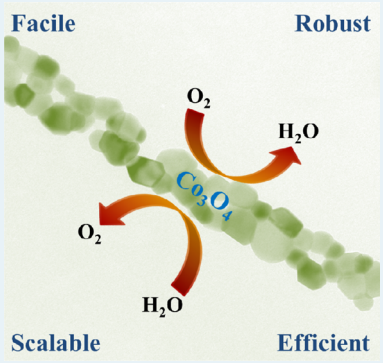

KEYWORDS: *multifunctional catalyst, cobalt oxide, oxygen evolution, water oxidation, oxygen reduction, morphology*

1. INTRODUCTION

The development of low-cost, naturally abundant, environmentally benign, and highly active catalysts for energy conversion and storage is of utmost importance and plays a prime role in renewable energy technologies.[1−5] In this context, the discovery of robust materials for the oxygen evolution reaction (OER) and oxygen reduction reaction (ORR), that is, suitable materials for the challenging reactions of water splitting, fuel cells, metal−air batteries, electrolysis cells, and solar synthetic reactors, is of particular interest.[6−13] The OER involves a four-step oxidation of water to molecular oxygen and has been widely used as an anodic reaction in electrolysis cells, whereas the ORR also supports four-electron reduction of oxygen and is ubiquitous for cathodic reactions in fuel cells.[14−17] Despite enormous efforts, the development of oxygen electrode catalysts is still a challenge, since high-performance electrocatalysts are mostly based on expensive and noble metals. The best known catalysts of OER are based on iridium or ruthenium oxides,[18−26] while their activity in the ORR is very moderate.[27] However, platinum-based materials have been most efficient for ORR[11,28−33] but are less effective for the reverse reaction, OER.[34−36]

Over the years, various non precious metal based materials have been explored that display higher activities, either for OER or for ORR (unifunctional).[37−45] Nevertheless, a single catalyst used as bifunctional in both OER and ORR is scarce, as the bifunctionality requires significantly low overpotentials and high activities for both reactions. Recently, the development of low-cost, high-performance, and non precious metal electrocatalysts have been realized with bifunctionality, especially with transition-metal oxide and sulfide materials based on cobalt and manganese.[46−50] Jaramillo et al. have shown the electrocatalytic activities of nanostructured manganese oxides as a bifunctional catalyst for both OER and ORR with higher activity which they compare to that of other noble metal catalysts.[46,51] Yang et al. described well-dispersed Co_3O_4/Co_2MnO_4 oxide nanocomposites as synergistic bifunctional catalysts that showed moderate activity toward OER and ORR.[52] Similarly, Cheng et al. synthesized spinels by rapid room-temperature synthesis and then directed for bifunctional catalysis.[53] Meanwhile, Joo et al. performed OER/ORR catalysis on ordered mesoporous Co_3O_4,[54] whereas Yang et al. explored $NiCo_2O_4$ for the same purpose.[55] Interestingly, Muhler et al. designed a spinel cobalt manganese oxide in N-doped carbon nanotubes by oxidative

Received: November 3, 2014
Revised: February 16, 2015
Published: February 16, 2015

DOI: 10.1021/cs501724v
ACS Catal. 2015, 5, 2017−2027

cutting that showed superior activity for both OER and ORR and was comparable that of to noble metal platinum, iridium, and ruthenium oxide catalysts.[56] Earlier, Manthiram et al. presented lithium cobalt oxides as potential bifunctional catalysts for metal−air batteries,[57] while the dual nature of nanostructured MnO_2 and its structure−property relation was studied by Suib et al.[48] Although OER and ORR on perovskite type materials has been the main stream of interest of the group of Shao-Horn for a very long time,[58−62] recently, they were successful in decorating perovskites that exhibited high performance in both directions.[63] On the other hand, some of the hybrids of transition metal oxides and sulfides grown on graphene have also been investigated lately, in which the cobalt oxide on nitrogen (N) doped graphene as synergistic catalyst, reported by Dai et al.,[64] and the cobalt monooxide with crumpled graphene have been shown to be very efficient toward both OER and ORR.[65] The $CoFe_2O_4$ with graphene nanohybrid for OER/ORR has also been shown to be effective by Strasser et al.[66] Although bifunctional catalysts have been rarely reported, multifunctional catalysts for electrochemical OER at both alkaline and neutral pH, oxidant-driven and photochemical water oxidation as well as for the ORR have never been obtained until now. Therefore, it has been particularly challenging to design and to develop high-performance multifunctional catalysts which are capable of unifying the OER and ORR for energy conversion and storage applications.

The recent perspective article of Lewis and Gray clearly reveals the essential factors in commercializing solar fuel technologies, where they state that it is not sufficient to design devices for solar fuels but rather efforts have to be made to control certain constraints involved in the viable integrated system.[67] According to them, efficiency, stability, and scalability are three main system requirements that are needed to overcome constraints. In this respect, we directed ourselves to have a catalyst that is not only highly active but also highly stable, facile, robust, and easily scalable.

Our recent activities in the area of bioinspired water oxidation catalysts and the production of highly active OER and ORR catalysts on a larger scale fostered us to explore the single-source precursor (SSP) approach toward the preparation of a multifunctional cobalt oxide catalyst.[68−73] In general, the SSP route can be very advantageous due to the relatively low temperature synthesis and precise control of the composition and of the oxidation states of the metals in the system. Moreover, the SSP approach allows us to have control of the morphology and electronic properties of desired materials that can be tuned by molecular design.[74−79] Here we report the unification of high-performance OER and ORR catalysis in the cobalt oxide material, employing the inverse micelle precursor approach to generate nanochains.

In the present work, nanochains of cobalt oxide (Co_3O_4) were synthesized by relatively low temperature degradation of the cobalt oxalate dihydrate ($CoC_2O_4{\cdot}2H_2O$) precursor, which turned out to serve as a highly active multifunctional catalyst for electrochemical OER and for oxidant-driven and photochemical water oxidation as well as for ORR. In fact, the as-prepared Co_3O_4 nanochains show excellent electrocatalytic OER activity at low overpotentials in both alkaline and neutral medium and also high performance in oxidant-driven and photochemical water oxidation. We additionally synthesized nanostructured Co_3O_4 under solvothermal conditions as well as compared the activities of commercially available cobalt oxides of various morphologies to show why the presented nanochain morphology is essential in order to achieve activity higher than that of the other nanotypes. Strikingly, the ORR activity of carbon-supported Co_3O_4 nanochains exhibits high performance which is comparable to that of the carbon-supported platinum system in alkaline medium. In addition to this, it is now possible to directly compare the oxygen redox catalysis performance of Co_3O_4 under different operating conditions.

2. RESULTS AND DISCUSSION

The cobalt oxalate precursor was synthesized via an inverse micelle approach. Thereafter, the formed oxalate precursor was thermally treated at a relatively lower temperature to produce the Co_3O_4 phase. The physical properties of both the precursor and the oxide were systematically investigated by powder X-ray diffraction (PXRD), inductively coupled plasma atomic emission spectroscopy (ICP-AES), elemental analyses, scanning electron microscopy (SEM), transmission electron microscopy (TEM), energy dispersive X-ray spectroscopy (EDX), Fourier transform infrared spectroscopy (FT-IR), Raman spectroscopy, nitrogen adsorption−desorption Brunauer−Emmett−Teller analysis (BET), thermogravimetric analysis (TGA), temperature-programmed reduction (TPR), and X-ray photoelectron spectroscopy (XPS). Details on the instrumental part are given in the Supporting Information.

All reflections obtained from the precursor by PXRD could be indexed on the basis of an orthorhombic phase of $CoC_2O_4{\cdot}2H_2O$ (JCPDS 25-0250, space group *Bbmb*), whereas the reflection peaks of the oxide phase were solely attributed to the cubic cell of Co_3O_4 (JCPDS 42-1467, space group *Fd*3*m*) with a lattice constant of 8.08 Å (Figures S1 and S2 in the Supporting Information). The crystal structure of $CoC_2O_4{\cdot}2H_2O$ consists of one-dimensional chains with each cobalt atom coordinated by two bidentate oxalate ligands and two water molecules and the Co_3O_4 has a normal spinel AB_2O_4 ($Co^{2+}Co_2^{3+}O_4$) structure in which the Co atoms are distributed among the tetrahedral (A) and octahedral (B) sites (Figure S3 in the Supporting Information).[80] Further, SEM and TEM images displayed that the one-dimensional nanorods of the precursor have been completely transformed to Co_3O_4 after the thermal treatment (Figure S4 in the Supporting Information). The chemical composition and the quantification of the elements of lower atomic number (C, H, N) of both precursor and as-prepared oxide was confirmed by EDX, ICP-AES, and elemental analysis (Figure S5 and Tables S1 and S2 in the Supporting Information). The thermal degradation of the precursor was examined by TGA (Figures S6 and S7 in the Supporting Information) that exhibited two-step mass loss corresponding to two structural water molecules and liberation of carbon dioxide before complete transformation into CoO and Co. The FT-IR and Raman spectra of the precursor and oxide are characteristic for metal oxalates and metal oxides (Figures S8−10 and Table S3 in the Supporting Information). SEM and TEM images of Co_3O_4 revealed that the material consists of small edge-sharing nanocrystals (20−60 nm) that form an unprecedented network of nanochains (Figure 1). The BET surface area of 16 m^2/g for the oxalate precursor was found to be congruent with the oxide phase (12 m^2/g). The TPR was conducted to study the reduction behavior of cobalt oxide which shows that Co_3O_4 undergoes a two-step reduction process (CoO and Co) between 300 and 600 °C; related details are given in Figure S11 in the Supporting Information.

DOI: 10.1021/cs501724v
ACS Catal. 2015, 5, 2017−2027

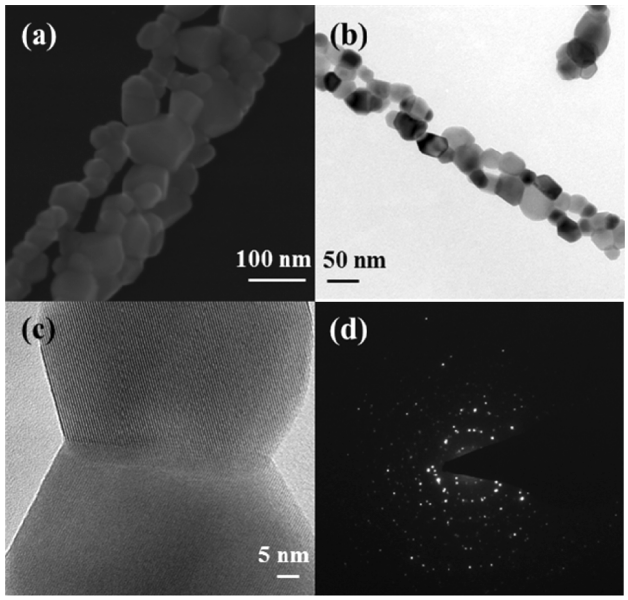

Figure 1. SEM (a) and TEM (b) images of Co_3O_4 nanochains, edge-sharing of the nanoparticles with lattice planes (c), and the electron diffraction pattern (d).

The detailed bonding states of the Co(II) oxalate precursor and Co(II,III) oxide materials were further characterized by XPS measurements. The Co(II) and Co(III) sites have almost similar 2p binding energies, but ultimately, they can be differentiated by the Co $2p_{1/2}$−$2p_{3/2}$ spin−orbit level energy spacing.[81] This difference is 16.0 eV for high-spin Co(II) and 15.0 eV for low-spin Co(III) and matches perfectly with values for synthesized Co(II) precursor and Co(II,III) oxide.[82] The binding energies of cobalt for the oxalate precursor were found to be 797.3 eV for Co $2p_{1/2}$ and 781.3 for Co $2p_{3/2}$ and are consistent with Co(II). The O 1s binding energy peaks can be deconvoluted into two different carbon−oxygen functional groups. The peak at 533.9 eV corresponds to the binding energy of a C−O bond or water ligands, and the peak at 532.2 eV could be assigned to the C═O bond. The deconvoluted C 1s spectrum comprises of three binding energy peaks at 284.9, 286.4, and 288.8 eV. The peaks at 284.9 and 286.4 eV are attributed to the carbon in C−C and C−O environments. The peak at 288.8 eV could be assigned to the C═O from the oxalate anion.[83,84] The corresponding results of Co 2p, O 1s, C 1s spectra are presented in Figure S12 in the Supporting Information.

For Co_3O_4 nanochains, two peaks are located at binding energies of about 780.0 eV for Co $2p_{3/2}$ and 795.1 eV for Co $2p_{1/2}$. The Co $2p_{3/2}$−$2p_{1/2}$ energy separation is approximately 15.1 eV, which is consistent with the literature--reported values of Co(II,III).[81,85] The absence of the prominent shakeup satellite peaks in the Co 2p spectra indeed suggests the presence of a dominating Co_3O_4 phase. The O 1s spectrum is deconvoluted into three main peaks. The peaks at 530.1, 531.8, and 533.0 eV are correlated to the oxygen atoms of cobalt oxide, physisorbed and chemisorbed water at or near the surface, and the hydroxide species, respectively.[86−88] The overview of Co 2p and O 1s spectra are shown in Figure 2.

Thin films of Co_3O_4 nanochains were first deposited on the FTO surface (Figure S13 in the Supporting Information), and the OER catalytic activity was measured in 0.1 M KOH (pH 13) and 0.1 M phosphate buffer (pH 7) solutions. To illustrate

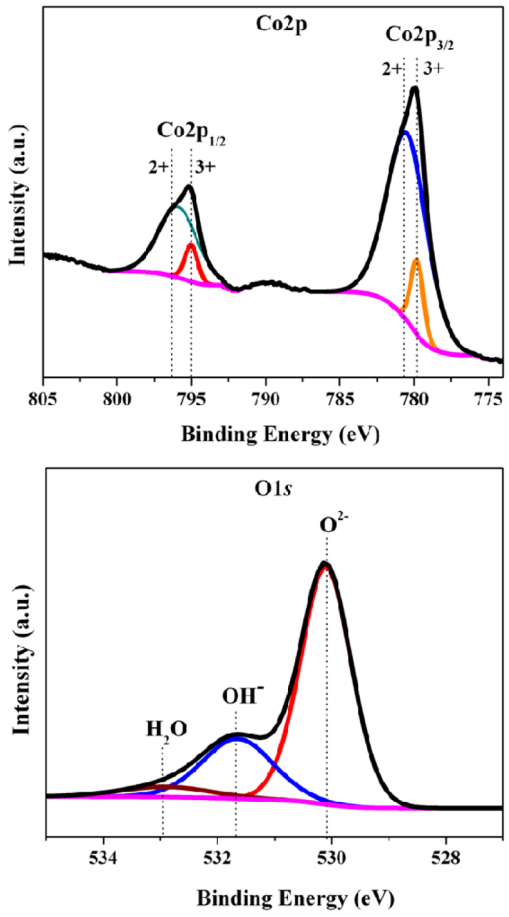

Figure 2. Co 2p (top) and O 1s (bottom) XPS spectra of nanochains of Co_3O_4.

the catalytic activity for OER and ORR, the linear sweep in the potential ranging from −0.5 to 2 V vs RHE was measured in the anodic direction, as shown in Figure 3. During initial

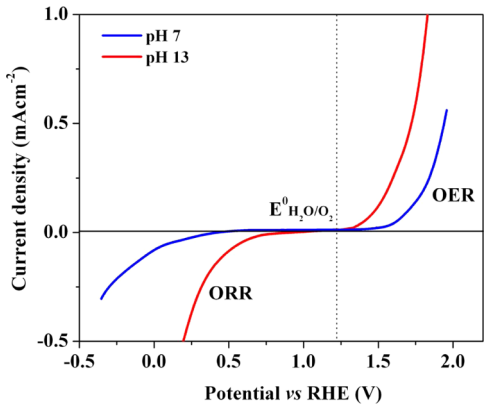

Figure 3. Linear sweep voltammetry at 1 mV/s in 0.1 M KOH at pH 13 and 0.1 M phosphate buffer at pH 7 (the results shown are the average of the forward and backward scans).

scanning at 1 mV/s, the Co_3O_4 thin film was found to be highly active for OER with low overpotential in KOH as well as in phosphate buffer solution. The current-onset overpotential displayed here is better than those of the well-established benchmark CoPi catalyst (0.28 V at pH 7), cobalt-based oxides, and other highly active catalysts based on precious metals.[89−99]

DOI: 10.1021/cs501724v
ACS Catal. 2015, 5, 2017−2027

A pronounced activity was also observed for ORR in basic medium by applying the reverse potential under the same conditions (note that ORR was performed in air-saturated solutions at ambient pressure). In order to understand both OER and ORR phenomena, the thin films of Co_3O_4 were investigated separately by the traditional established routes to evaluate the actual performance.

Figure 4 shows the cyclic voltammograms (CVs) measured at a scan rate of 20 mV/s. The anodic current started growing

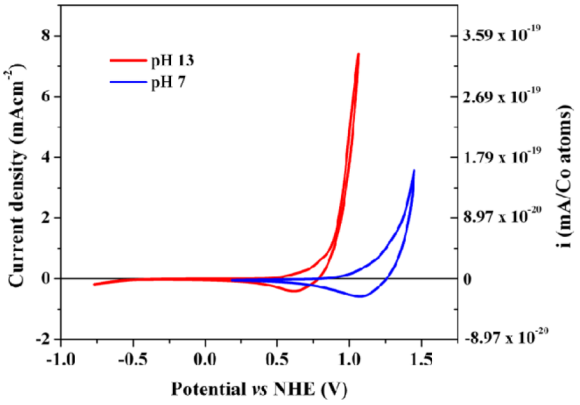

Figure 4. Cyclic voltammograms (sweep rate 20 mV/s) of nanochains of cobalt oxide thin films in 0.1 M KOH (pH 13) and 0.1 M phosphate buffer solution (pH 7).

at 0.66 V at pH 13 and 1.05 V at pH 7 (vs the normal hydrogen electrode, NHE). The maximum current density of 7.4 mA cm^{-2} was attained at 1.06 V at pH 13, whereas 3.6 mA cm^{-2} at 1.44 V was observed at pH 7. It can be seen that the synthesized Co_3O_4 nanochains are highly active for OER and the current densities start growing at very low onset potentials. The overpotentials obtained here are superior than those of most of the known benchmark transition-metal oxide water oxidation catalysts.[100−106]

The pH dependence of the electrode potential at three anodic current densities, 3, 10, and 30 μA cm^{-2}, were also studied at pH 7 in phosphate buffers (Figure 5). The plots show a slope of 60 mV per pH unit and thus indicate a pH-independent electrochemical overpotential, as previously found

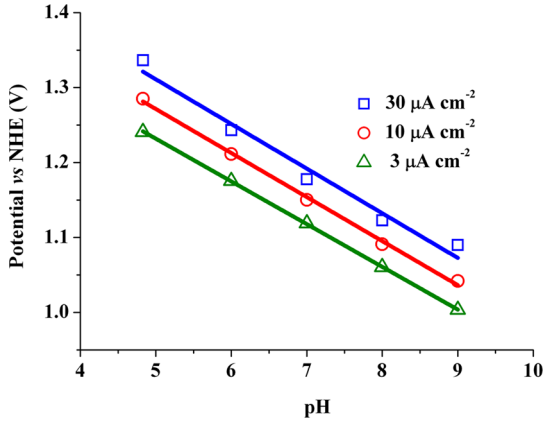

Figure 5. pH dependence of the electrode potential of the Co_3O_4 film measured at three anodic current densities (in 0.1 M phosphate buffer). The solid lines correspond to a slope close to 60 mV/pH unit, indicating a fully pH independent electrochemical overpotential.

also in other water oxidation catalysts based on first-row transition metals.[41,89−91,107]

Furthermore, the stability of the Co_3O_4 thin films was confirmed by chronopotentiometric measurements at a current density of 0.5 mA cm^{-2} over a 1 h period, resulting in overpotentials of 0.34 and 0.51 V at pH 13 and pH 7 (Figure S14 in the Supporting Information). After the chronopotentiometric test, the films were characterized by SEM, TEM, and XPS analyses (Figure 6 and 7 and Figures S15−S17 in the

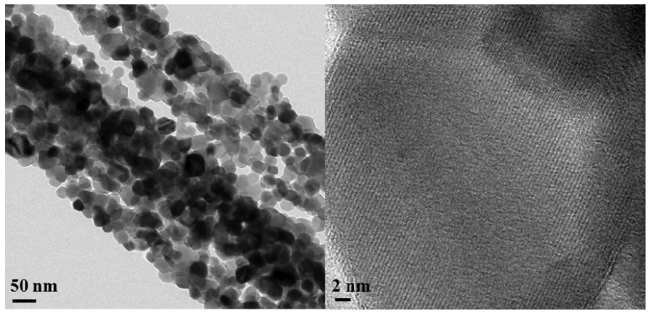

Figure 6. TEM (left) and HRTEM (right) images of the surface of Co_3O_4 thin film after chronopotentiometric measurements in 0.1 M KOH solution (pH 13).

Supporting Information). The SEM images of both films showed that the nanochains of Co_3O_4 stayed mostly intact and

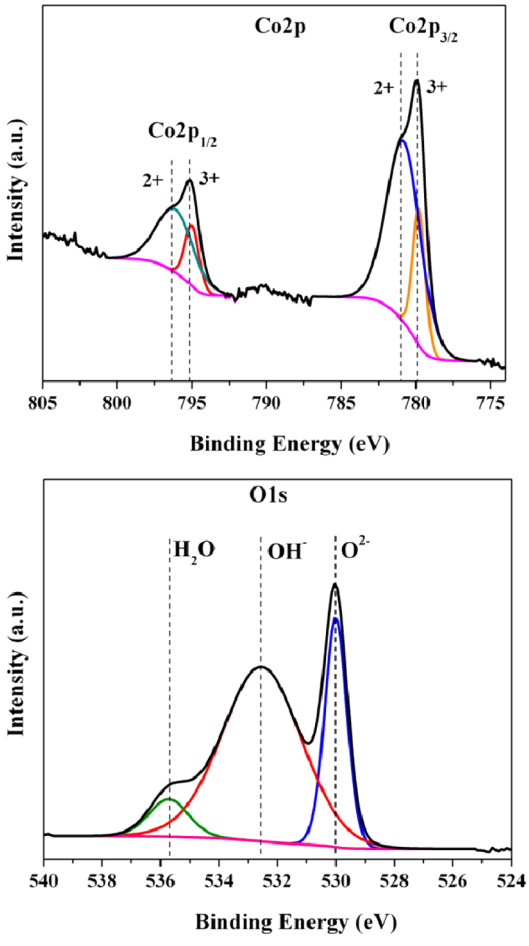

Figure 7. XPS spectra of the nanochains of Co_3O_4 thin film after chronopotentiometric measurements in 0.1 M KOH (pH 13) solution.

DOI: 10.1021/cs501724v
ACS Catal. 2015, 5, 2017−2027

no distinct changes in the surfaces of the films were discerned by preserving the morphology and crystallinity. A closer look at the TEM images (Figure 6) revealed that there is no visible amorphous layer formation on the surface of the film or detectable dissolution from the surface as reported for other materials.[108−110] However, the Co 2p spectrum in XPS exhibited a significant increase in Co^{3+} character (~780 eV at Co $2p_{3/2}$ and ~795 eV at Co $2p_{1/2}$) from the deconvolution area which shows that a large amount of surface Co^{2+} in the structure of $Co^{2+}Co_2^{3+}O_4$ has been oxidized to Co^{3+} (Figure 7 and Figure S17). The corresponding O 1s core level spectrum also indicated possible structural changes and was deconvoluted into three peaks. The peaks at 530 eV could be assigned to the oxygen atoms of Co_3O_4, whereas a large dominance of −OH species absorbed on the surface were observed at the binding energy of 532.1 eV. A small peak at around 535.5 eV can be correlated to the absorbed water molecules.[86−88]

It is essential to compare the OER activities of nanochains of cobalt oxide synthesized by the reverse micelle route to those of other cobalt oxides with various morphologies (Figures S18 and S19 in the Supporting Information). Therefore, we solvothermally synthesized a Co_3O_4 catalyst (18 m^2/g) that displayed cubic type morphology. In addition to this, we evaluated the activities of commercially available Co_3O_4 (49.4 m^2/g) and CoO (25.5 m^2/g). The commercial Co_3O_4 particles display irregular shaped morphology, whereas CoO exhibits multifaceted particles.

The OER activities of the solvothermally synthesized and commercial cobalt oxides were measured under conditions similar to those of Co_3O_4 nanochains prepared by micelle and are shown in Figure 8. The current-onset potential of

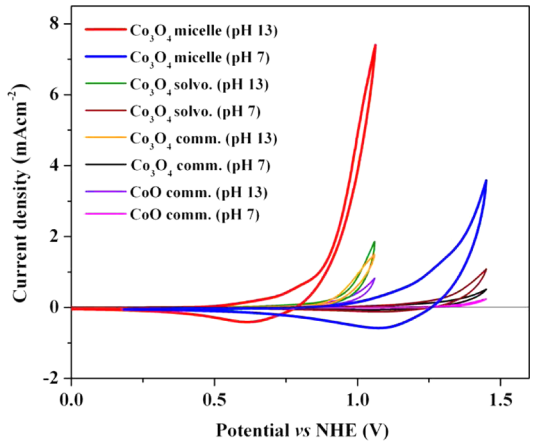

Figure 8. Cyclic voltammograms (sweep rate 20 mV/s) of Co_3O_4 synthesized under micelle and solvothermal conditions along with commercial Co_3O_4 and CoO in 0.1 M KOH (pH 13) and 0.1 M phosphate buffer (pH 7) solution (catalyst loading is 3 mg cm^{-2}).

solvothermal cube-shaped Co_3O_4 nanoparticles started at 0.45 and 0.60 V and reached a current density of 1.83 mA cm^{-2} at 1.05 V and 1.11 mA cm^{-2} at 1.45 V for pH 13 and pH 7, respectively. Similarly, in the case of irregularly shaped commercial Co_3O_4 and multifaced CoO particles, a significant increase in the respective current-onset potential was observed, which started at ~0.66 and ~0.58 V and reached a maximum current density of 1.47 and 0.83 mA cm^{-2} at 1.05 and 1.06 V for pH 13. In the case of pH 7, the current started growing at considerably higher potentials: i.e, 0.95 and 0.80 V for commercial Co_3O_4 and CoO. The maximum current densities achieved here were 0.50 and 0.30 mA cm^{-2} at 1.44 V.

The overpotentials determined at 0.5 mA cm^{-2} from the CV of Figure 8 are displayed in Table 1, indicating that the

Table 1. Summary of the OER Catalytic Activities of Cobalt Oxides of Various Morphologies

		overpotential (mV) at 0.5 mA cm^{-2}	
catalyst	S_{BET} [c]	pH 13	pH 7
Co_3O_4 micelle	12	320	410
Co_3O_4 solvo[a]	18	511	590
Co_3O_4 comm[b]	49.4	531	630
CoO comm[b]	25.5	572	-

[a]Solvothermal. [b]Commercial. [c]Surface area (m^2/g).

nanochains of Co_3O_4 have overpotentials much lower than those of the solvothermally synthesized and commercial cobalt oxides of various morphologies at both pH 13 and pH 7.

Oxidant-driven water oxidation experiments (see the Experimental Section) were carried out in deoxygenated aqueous solution containing Co_3O_4 nanochains and ceric ammonium nitrate (CAN). The standard chemical potential of Ce(IV) (E° = 1.7 V vs NHE) is quite sufficient to oxidize water to oxygen under acidic conditions. Figure 9 shows the dissolved

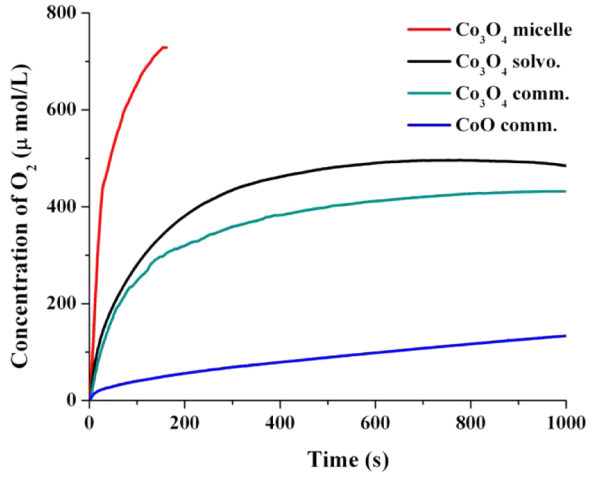

Figure 9. Dissolved oxygen concentrations measured with a Clark electrode in deoxygenated aqueous solutions containing cobalt oxide catalysts and 0.5 M ceric ammonium nitrate (CAN) as an oxidant (catalyst amount is 1 mg).

oxygen content in the reactant solution monitored for 15 min at room temperature. The rate of the oxygen evolution was determined from the slope of the linear fitting for the first 60 s and was found to be 1.49 $mmol_{O_2}$ mol_{Co}^{-1} s^{-1}. Similarly, the CAN experiments were also carried out for solvothermally synthesized Co_3O_4 (0.59 $mmol_{O_2}$ mol_{Co}^{-1} s^{-1}), commercial Co_3O_4 (0.51 $mmol_{O_2}$ mol_{Co}^{-1} s^{-1}), and CoO (0.08 $mmol_{O_2}$ mol_{Co}^{-1} s^{-1}). The rates of oxygen evolution for Co_3O_4 nanochains were 3 times higher than that of cubic nanoparticles, whereas commercial materials showed moderate activity (see Table 2). In addition, the value obtained here for nanochains is higher than those of other known reported cobalt oxides and the supported cobalt oxide catalysts (highest

DOI: 10.1021/cs501724v
ACS Catal. 2015, 5, 2017−2027

Table 2. Summary of the Oxidant-Driven and Photochemical Activities of Cobalt Oxide Catalysts

		O_2 evolution rate ($mmol_{O_2}$ mol_{Co}^{-1} s^{-1})	
catalyst	S_{BET}[c]	oxidant driven	photochemical[d]
Co_3O_4 micelle	12	1.49	1.45
Co_3O_4 solvo[a]	18	0.59	0.59
Co_3O_4 comm[b]	49.4	0.51	0.29
CoO comm[b]	25.5	0.08	0.08

[a]Solvothermal. [b]Commercial. [c]Surface area (m^2/g). [d]Measured in phosphate buffer. The oxygen evolution rate was determined for the first 60 s.

known 0.60 $mmol_{O_2}$ mol_{Co}^{-1} s^{-1} for KIT-6 supported Co_3O_4).[111−115]

The photocatalytic activity of water oxidation for the Co_3O_4 nanochains was investigated in the presence of a two-electron acceptor ($Na_2S_2O_8$) and a photosensitizer ($[Ru(bpy)_3]^{2+}$) in various buffer solutions (Scheme S1 in the Supporting Information).[43,101,116,117] In the $Ru(bpy)_3]^{2+}$−$S_2O_8^{2-}$system, $[Ru(bpy)_3]^{2+}$ absorbs visible light and generates electron−hole pairs on the surface of the catalyst. The electrons produced were ejected by the sacrificial electron acceptor $S_2O_8^{2-}$ by further oxidizing the $[Ru(bpy)_3]^{2+}$ to $[Ru(bpy)_3]^{3+}$ and reducing $S_2O_8^{2-}$ to SO_4^{2-} and a sulfate radical ($SO_4^{\bullet-}$). As a result, the formed radical can subsequently further oxidize $[Ru(bpy)_3]^{2+}$ to yield $[Ru(bpy)_3]^{3+}$. Hence, the $[Ru(bpy)_3]^{3+}$ molecule donates its holes to the catalyst and reverts back to $[Ru(bpy)_3]^{2+}$, where two water molecules are oxidized to form one oxygen molecule. The dissolved O_2 content was analyzed by a Clark oxygen electrode system. The maximum rate of oxygen evolution of nanochains of Co_3O_4 was calculated as 1.45 $mmol_{O_2}$ mol_{Co}^{-1} s^{-1} in phosphate buffer (Figure 10) and,

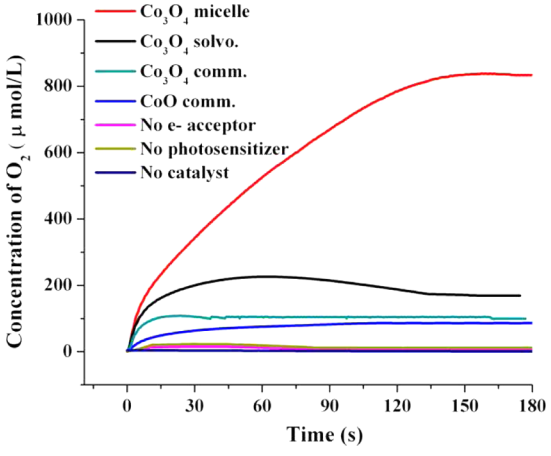

Figure 10. Dissolved oxygen concentration of cobalt oxide (0.5 mg) catalysts measured by a Clark electrode in the $S_2O_8^{2-}$−$Ru(bpy)_3^{2+}$ system using phosphate (pH 7) buffer (300 W Xe lamp with 395 nm cut off filter).

remarkably, is clearly larger than that of previously reported cobalt oxides (6 times higher than that of the recently reported active mesoporous Co_3O_4) and comparable to that of cobalt oxide supported on silica.[111,115,118,119]

Measurements were performed to check the effect of catalytic activity and stability in various buffer solutions, including carbonate (pH 4.7), acetate (pH 5.8), phosphate (pH 7), and borate (pH 9), and are shown in Figure S20 in the Supporting Information. Using the borate buffer, especially high rates of O_2 formation were detected in the presence of the Co_3O_4 nanochains, but significant rates were detectable also in the absence of the Co_3O_4 catalyst (Figure S21 in the Supporting Information), the latter likely being explainable by photosensitizer degradation and formation of catalytic RuO_2, due to the high oxidation potential of $[Ru(bpy)_3]^{3+}$ at pH 9. Therefore, the phosphate buffer was chosen to get the best results in terms of stability as well as catalytic activity. Clearly, less oxygen evolution was detected for solvothermally synthesized (0.59 $mmol_{O_2}$ mol_{Co}^{-1} s^{-1}) and commercially available cobalt oxide (0.29 $mmol_{O_2}$ mol_{Co}^{-1} s^{-1}) and cobalt monoxide (0.08 $mmol_{O_2}$ mol_{Co}^{-1} s^{-1}), even though the surface area was much higher for the commercial oxides (Figure 10 and Table 2).

The oxygen evolution trend displayed in photocatalytic experiments is also very similar to that of oxidant-driven water oxidation. The corresponding surface area normalized plots for all cobalt oxides are shown in Figure S22 in the Supporting Information. No oxygen was detected when the catalysts were not present in the photochemical reaction.

In a separate set of experiments of nanochains of Co_3O_4 in phosphate buffer (see the Supporting Information), the oxygen gas collected in the head space of the reaction mixture was quantitatively analyzed by a gas chromatograph (GC). A maximum oxygen yield of 0.05 mL h^{-1} of O_2 was detected (Table S4 in the Supporting Information). $H_2{}^{18}O$ labeling studies on Co_3O_4 were also performed using a GC equipped with a mass spectrometer, which confirm that water is the source of the evolved dioxygen (Figure S23 in the Supporting Information).

After the oxidant-driven and photochemical water oxidation of highly active Co_3O_4 nanochains, the products obtained were washed thoroughly with water and subjected to PXRD, TEM, EDX, and XPS (Figures S24−S28 in the Supporting Information) analysis. PXRD and TEM revealed that the morphology and the crystallinity of the nanochains were preserved even after treatment with CAN as well as after photolysis. EDX measurements of the products after both reactions confirm the presence of only cobalt without any additional elements. The Co 2p spectrum in XPS confirmed the oxidation states of cobalt and showed a dominating increment of Co^{3+} character as displayed for electrochemical OER. The deconvoluted O 1s spectrum displayed three peaks related to oxygen atoms of Co_3O_4 (~530 eV), −OH species absorbed on the surface (~532 eV), and chemisorbed oxygen or adsorbed water molecules (~534 eV).[86−88] The increase in the −OH peak in the O 1s spectrum is possibly due to the changes in the surface groups and in the bulk material.

We further compared the trend followed for the oxygen production in photochemical (for 60 s) and electrochemical (at 1.45 V vs NHE) water oxidation experiments at pH 7, by taking their respective ratios. In both experiments, the ratios of oxygen formation matched closely, indicating that the nanochains of Co_3O_4 are indeed suitable catalysts to drive both reactions efficiently, even though different mechanisms are involved in the processes of photochemical and electrochemical OER.

Furthermore, we prepared the corresponding oxalate precursor without the micelle route, which was then subjected to thermal treatment to form spherically dispersed particles of cobalt oxide (Figure S29 in the Supporting Information). The oxidant-driven and the photocatalytic tests on the spherical

DOI: 10.1021/cs501724v
ACS Catal. 2015, 5, 2017−2027

particles confirmed that the edge-sharing nanochains have significantly higher activity, evidencing the importance of morphology in the catalytic activity (Figures S30 and S31 in the Supporting Information).

Since the nanochains of Co_3O_4 exhibited very high performance for electrochemical OER and oxidant-driven and photochemical water oxidation, we considered exploring this catalyst further in the direction of ORR. It is already well known that the unsupported transition metal oxide nanoparticles do not show a well-defined diffusion part at more negative potentials due to the poor transfer of substrate (O_2) and products (H_2O). Usually, in the case of non precious metal based electrocatalysts, especially for those with low electrical conductivity, mixing of carbon provides paths for the flow of electrons in the electrocatalytic system.[120−122] Therefore, the nanochains of Co_3O_4 were first mixed with carbon black (Vulcan XC-72R) to overcome electronic conductivity limitations.

To evaluate the ORR activity, linear sweep voltammetry (LSV) of carbon-supported Co_3O_4 nanochains (20 wt % Co_3O_4 on Vulcan X-72) was recorded using a rotating-disk electrode (RDE) in O_2-saturated 0.1 M KOH solution with a sweep rate of 10 mV/s and were compared with commercial carbon-supported Pt benchmark catalysts with a Pt loading of 20% by weight. Figure 11 evidences that the ORR activity of the

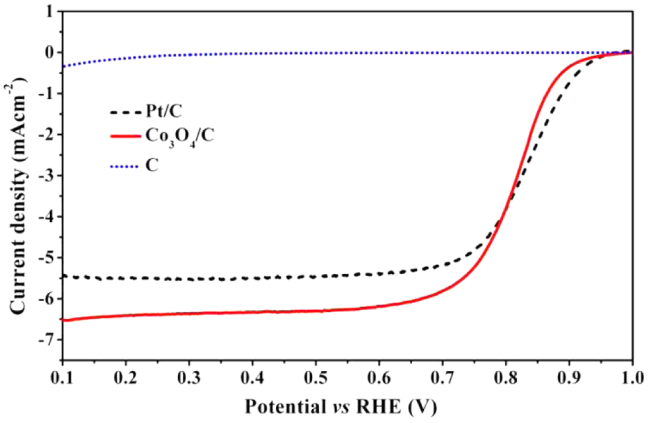

Figure 11. Linear sweep voltammograms (LSVs) of nanochains of Co_3O_4/C and Pt/C and C (Vulcan) in oxygen-saturated 0.1 M KOH with a scan rate of 10 mV/s (at 1500 rpm, the Co_3O_4 loading is 45 μg cm^{-2}).

Co_3O_4/C catalyst in the kinetic region between 0.8 and 0.95 V approaches that of the Pt reference catalyst. Differences in catalyst film thickness accounted for the varying diffusion-limited current densities below 0.75 V. The electrochemical half-wave potential of Co_3O_4/C, a key activity metric, was 0.84 V and is very similar to the reference Pt/C (0.86 V) catalyst better than a recently reported highly active N-doped graphene supported Co_3O_4 (0.83 V) and CoO catalysts (0.81 V).[64,65] In addition, the potential assessed by the nanochains of Co_3O_4/C reported herein represents oxygen reduction capacity clearly higher than that detected in any other nanostructured cobalt-containing oxides, including so far known highly active mesoporous Co_3O_4/C,[54] Co_3O_4/graphene,[123] Co_xO_y embedded N-doped carbon,[124] Mn−Co oxide carbon nanotubes,[56] 3D crumpled graphene cobalt oxide,[65] lithium cobalt oxide,[57] and covalent hybrids of Mn−Co/graphene catalysts[125] as well as Co_3O_4/N-doped graphene.[64]

A high-performance ORR catalyst not only must show an enhanced activity but also must be stable under ORR conditions.[126,127] The chronoamperometric curve of presented Co_3O_4/C is shown in Figure S32 in the Supporting Information. The catalysts maintained 93.6% and 93% of their initial ORR current values for over 2 h of continuous operation at a constant potential of 0.8 V. After chronoamperometric tests, the Co_3O_4 catalyst showed an overpotential increase commensurate with that of benchmark catalysts (Figure S33 in the Supporting Information).

The number of transferred electrons (n) is a key parameter while evaluating the selectivity of the catalysts in ORR. The RDE current−potential curves of Co_3O_4/C with various rotation speeds (800−2200 rpm) were recorded at a scan rate of 10 mV/s and are presented in Figure 12.

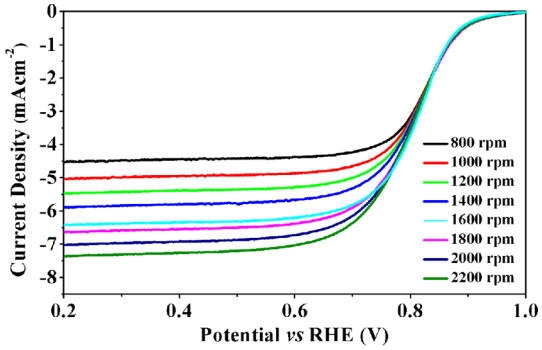

Figure 12. LSVs of Co_3O_4/C in oxygen-saturated 0.1 M KOH at different electrode rotating rates at a scan rate of 10 mV s^{-1}.

Additional kinetic analyses using the Koutecky−Levich (K-L) formalism of the Co_3O_4/C catalyst addressed the number of transferred electrons (Figure 13; see the Supporting

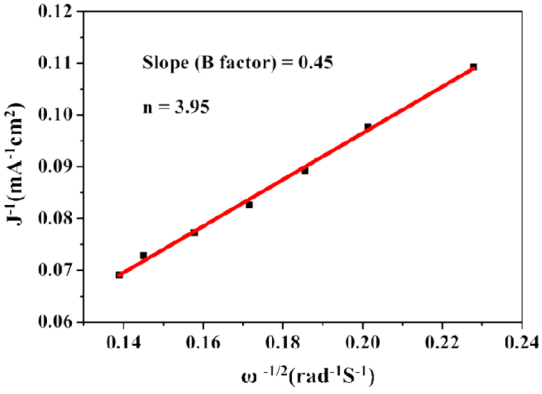

Figure 13. Koutecky−Levich (K-L) plot for ORR in O_2-saturated 0.1 M KOH solution for Co_3O_4/C. The calculated slope was 0.45 (B). The experimental "B factor" was calculated and averaged at various voltages from the slope of the K-L plot.

Information for the equation). The K-L plots are obtained from the inverse current density J^{-1} as a function of the inverse square root of the rotation rate ($\omega^{1/2}$). The slope of the straight line from a K-L plot referred to as a "B factor" was 0.455 mA cm^{-2} $S^{1/2}$ for Co_3O_4/C (the theoretical "B factor" for a direct four-electron process is 0.46 mA cm^{-2} $S^{1/2}$). This shows that the calculated electron number is 3.95 for Co_3O_4/C that favors the 4e oxygen reduction process similarly to the Pt reference catalyst.

DOI: 10.1021/cs501724v
ACS Catal. 2015, 5, 2017−2027

As already discussed, cobalt oxide has the normal spinel structure $Co^{2+}Co_2^{3+}O_4$, where Co^{3+} ion in the formula unit occupies the octahedral sites, while Co^{2+} ion is in the tetrahedral site.[128] In the crystal structure of Co_3O_4, the {001} and {111} planes (facets) are comprised of Co^{2+}, whereas the {110} plane consists of Co^{3+}.[123,129,130] It has been shown recently that the surface octahedral Co^{3+} site is the actual active site for OER and a similar trend has been seen in substituted cobalt oxides.[125] Further, the observation made by XANES has also suggested that Co^{3+} is indeed the active site of water oxidation of cobalt-based spinel-type materials.[131−133] In addition, Xie et al. and others have previously demonstrated that the {110} planes in cobalt oxide have the highest catalytic activity toward CO oxidation due to their highest density of Co^{3+} ions, which is in line with the presented results.[134,135] Conversely, Guo et al. investigated the surface structure dependent activity of various types of cobalt oxide nanoparticles and reported that the catalytic active sites for ORR should be from the surface of Co^{2+} (tetrahedral sites) ions that was followed by the presence of {111} lattice planes on the surface of the nanocrystals and could also be the case in the presented material.[123]

Furthermore, most of the high-performance catalysts of transition metal oxides were produced on a smaller scale that is difficult to scale up. The use of the single source precursor approach to nanochains of cobalt oxide enables us to explore high-performance catalysts for reversible oxygen redox catalysis and overcomes the problem of large scale production. Inexpensive and abundant starting materials and easier handling make this catalyst a prime candidate for heterogeneous water oxidation and oxygen reduction reactions and is an alternative to most of the conventional and strenuous synthetic catalysts. This method can easily be extended for other transition metals in designing and shaping catalysts, and interestingly, the result presented here fulfils the key requirements needed for the practical applications as described in the Venn diagram of Lewis and Gray.[67]

3. CONCLUSION

In conclusion, this is the first report that one and the same catalyst was tested, compared, and contrasted for electrochemical OER (at neutral and alkaline pH), oxidant-driven and photochemical water oxidation (at various pHs), and ORR in alkaline media. The multifunctional Co_3O_4 nanochains derived from the inverse micelle precursor approach exhibited superior activities and remarkable stability toward OER in both alkaline and neutral solution. In addition, retention of the crystallinity and morphology was observed even after chronopotentiometric measurements. In addition to the electrochemical OER experiments, oxidant-driven water oxidation in CAN solution and photochemical water oxidation in the $S_2O_8^{2-}$−$[Ru(bpy)_3]^{2+}$ system in various buffer solutions were investigated and the detected catalytic rates were clearly higher than the solvothermally synthesized, commercial cobalt oxides of various morphologies as well as the other transition metal based catalysts. The ORR was carried out in an alkaline medium, and results obtained here outperformed the benchmark of precious metal catalysts in terms of catalytic activity and chronoamperometric stability. For the first time, a direct comparison of the oxygen redox catalysis performance under different operating conditions was described. The employed precursor strategy opens a new avenue for the development of new materials which unifies properties in the field of energy materials. In addition, the synthesized Co_3O_4 nanochains can easily be scaled up commercially and can be designed for industrial applications.

4. EXPERIMENTAL SECTION

4.1. Synthesis of Oxalate Precursor. Microemulsions containing cetyltrimethylammonium bromide (CTAB, 2.0 g) as a surfactant, 1-hexanol (20 mL) as cosurfactant and hexane (35 mL) as the lipophilic phase were first prepared and were mixed separately with an aqueous solution of 0.1 M cobalt acetate and 0.1 M ammonium oxalate. Both microemulsions were mixed slowly and stirred overnight. The pink precipitate then obtained was centrifuged and washed with a 1/1 mixture of chloroform and methanol (200 mL) and subsequently dried at 60 °C for 12 h.

4.2. Synthesis of Cobalt Oxide Nanochains. The cobalt oxalate precursor was heated to 400 °C at a rate of 2 °C/min in dry synthetic air (20% O_2, 80% N_2) and kept at 400 °C for 8 h in a tubular furnace and then cooled to ambient temperature normally.

4.3. Solvothermal Synthesis of Cobalt Oxide Cubic Particles. In a beaker, 2 g of cobalt acetate tetrahydrate was dissolved in 35 mL of water. A 5 mL portion of 25% NH_3 solution was added to the above solution, which was then transferred into a 50 mL Teflon autoclave. The autoclave was heated to 180 °C for 24 h and subsequently cooled to room temperature. The product was washed with a water/acetone solution and dried at 60 °C in air.

4.4. Irregular Shaped and Multifaceted Cobalt Oxide Nanoparticles. The irregularly shaped Co_3O_4 and the multifaceted CoO nanoparticles were purchased and used as received from Sigma-Aldrich.

4.5. Oxidant-Driven Oxygen Evolution from Water. Chemical oxygen evolution experiments were carried out using aqueous solutions containing ceric ammonium nitrate (CAN) as the sacrificial one-electron acceptor. The oxygen evolution was measured using a Clark-type oxygen electrode system (Strathkelvin, 1302 oxygen electrode and 782 oxygen meters). Prior to the experiments, the electrode was calibrated in an air-saturated water solution and in zero oxygen (sodium sulfite in water) solution. In a typical reaction, 1 mg of the catalyst was placed in the reactor, which was then degassed by purging nitrogen for 30 min. An anaerobic solution (2 mL) of 0.5 M CAN was then injected into the reactor to initiate the chemical water oxidation, and oxygen evolution was monitored with a Clark electrode under stirring. In each case, the maximum rate of oxygen evolution was calculated using the amount of oxygen after the first 60 s of reaction.

4.6. Photocatalytic Oxygen Evolution from Water. Photochemical water oxidation experiments were performed in a 10 mL quartz reactor fitted with a water jacket by maintaining the temperature at 20 ± 0.5 °C. $Na_2S_2O_8$ was chosen as the sacrificial electron acceptor and $Ru(bpy)_3]^{2+}$ as the photosensitizer. Various buffer solutions, including carbonate (Na_2SiF_6−$NaHCO_3$; pH 4.7), acetate (CH_3COONa−CH_3COOH; pH 5.8), phosphate (Na_2HPO_4−KH_2PO_4; pH 7), and borate (H_3BO_3−$Na_2B_4O_7$; pH 9), were tested, and the phosphate buffer under neutral conditions was found to be most suitable, not only due to its stability but also because of its higher rates of oxygen evolution. A typical run was carried out using 1.5 mg of $[Ru(bpy)_3]Cl_2·6H_2O$, 3.5 mg of $Na_2S_2O_8$ and 1 mL of phosphate buffer along with 0.5 mg of catalyst. The reactants were purged with nitrogen for almost 1 h to remove

DOI: 10.1021/cs501724v
ACS Catal. 2015, 5, 2017−2027

all dissolved oxygen from the aqueous solution. The quartz reactor was then illuminated with a continuous output xenon lamp with a power of 300 W. Visible light was achieved by placing a long-pass filter of 395 nm between the quartz reactor and the light source. Dissolved oxygen formed during the reaction was measured by a Clark electrode, and the maximum rate of oxygen evolution was calculated similar to that of chemical water oxidation. All photochemical reactions were performed at least three times to ensure good reproducibility and reliability. Oxygen evolution was only observed when all constituents, i.e., the catalyst, the light source, the sacrificial electron acceptor, and the catalysts, were involved in the reaction. The catalytic activities were leveled after 3 min of photolysis due to the use of lower concentrations and the consumption of the sacrificial electron acceptor and decomposition of $[Ru(bpy)_3]^{2+}$. Replacing the solution with sacrificial acceptor and readjusting the pH to 7 resulted in continued water oxidation at the same rate, as known for previously studied materials.[69,70,111,136]

4.7. Oxygen Detection by GC. A separate set of controlled experiments were carried out under conditions similar to those above to quantify the oxygen gas in photochemical water oxidation by placing 30 mg of the catalyst, 25 mg of $[Ru(bpy)_3]Cl_2{\cdot}6H_2O$, 100 mg of $Na_2S_2O_8$, and 6 mL of phosphate buffer solution in a quartz reactor with a headspace of 15 mL. The reactor was then irradiated for 2 h using a xenon lamp (300 W, cut off filter 395 nm), and the O_2 molecules in the head space were sampled twice and quantitatively analyzed by a gas chromatograph (GC).

4.8. Oxygen Detection with $H_2{}^{18}O$ by GC-MS. Labeled oxygen studies were also performed using conditions similar to those for oxygen detection by GC. A 30 mg portion of catalyst, 25 mg of $Ru(bpy)_3]Cl_2{\cdot}6H_2O$, 100 mg of $Na_2S_2O_8$, 5.8 mL of phosphate buffer, and 0.2 mL of $H_2{}^{18}O$ solution were placed in a quartz reactor with a headspace of 15 mL. After an irradiation period of 2 h (300 W Xe lamp, cut off filter 395 nm), the resulting values of m/z 36 ($^{18}O^{18}O$), m/z 34 ($^{16}O^{18}O$), and m/z 32 ($^{16}O^{16}O$) were systematically monitored using a gas chromatograph equipped with a mass spectrometer (GC-MS).

4.8. Electrochemical Oxygen Evolution Reaction (OER). The catalytic activity of the cobalt oxide was tested in 0.1 M phosphate buffer (pH 7.0) and in freshly prepared 0.1 M KOH (pH 13.0) solution using a single-compartment three-electrode electrochemical cell. The working electrode was prepared by dissolving 3 mg of the Co_3O_4 powder in 2 mL of 2-propanol and then slowly drop-coating the solution on the fluorinated tin oxide (FTO) surface (~3 mg cm^{-2}). A few drops of 5 wt % Nafion were also drop-coated on the surface to ensure the enhancement of mechanical stability of the electrodes. A high-surface-area Pt mesh was used as the counter electrode and $Hg/HgSO_4$ (saturated) as the reference electrode. The electrochemical experiments were performed at room temperature using a potentiostat (SP-300, BioLogic Science Instruments) controlled by the EC-Lab v10.20 software package. Test runs were carried out with an electrolyte resistance (including the electrode) of about 40 Ω; *iR* compensation at 80% was applied. The solution was not stirred during the experiments. To investigate the pH dependence, chronopotentiometric measurements maintaining a preset current (3, 10, and 30 $\mu A\ cm^{-2}$) were performed.

4.9. Electrochemical Oxygen Reduction Reaction (ORR). Electrochemical measurements of the prepared catalyst were carried out in a standard three-electrode electrochemical glass cell connected to a Pine Potentiostat Instrument Company electrochemical analysis system at room temperature. The working electrode was a glassy-carbon (GC) disk (5 mm diameter), while RHE and platinum gauze were used as reference and counter electrodes, respectively. Freshly made 0.1 M KOH solution as the alkaline electrolyte was flushed with highly pure nitrogen and oxygen gases for measurements. The working electrode was coated with a 10 μL drop of the catalyst and dried at 60 °C to create a thin and homogeneous film on the electrode surface (9 μg). The ink formulation, which was optimized for these measurements, was the following: 5 mg of Co_3O_4/C (20 wt % of Co_3O_4 on Vulcan C) and 100 μL of 5 wt % Nafion were ultrasonically dispersed in 1 mL of a mixture of water and 2-propanol (5/1) for 15 min to form a homogeneous ink. The ORR activity of the prepared film was tested in an O_2-saturated solution with linear sweep voltammetry (LSV) with a scan rate of 10 mV s^{-1} at 1500 rpm. To investigate the selectivity of the ORR on the catalyst active sites for the four-electron pathway resulting in water production, the diffusion part was studied by recording LSV at different rotating speeds from 800 to 2200 rpm. Chronoamperometric stability tests were performed under a constant potential of 0.8 V vs RHE at a stationary electrode in N_2-saturated electrolyte for 6000 s. All of the results have been compared with the benchmark reference Pt/C (20 wt % Pt on Vulcan carbon, E-TEK) with a loading of 10 $\mu g\ cm^{-2}$.

■ ASSOCIATED CONTENT

Supporting Information

The following file is available free of charge on the ACS Publications website at DOI: 10.1021/cs501724v.

PXRD patterns, EDX spectra, ICP-AES analyses, IR spectra, Raman spectra, thermal analysis, TPR, SEM, TEM, BET, and XPS, all plots concerning oxidant-driven, photochemical, and electrochemical OER and ORR and characterizations after the electrochemical measurements (PDF)

■ AUTHOR INFORMATION

Corresponding Authors

*E-mail for P.S.: pstrasser@tu-berlin.de.
*E-mail for H.D.: holger.dau@fu-berlin.de.
*E-mail for M.D.: matthias.driess@tu-berlin.de.

Notes

The authors declare no competing financial interest.

■ ACKNOWLEDGMENTS

Financial support by the BMBF (L2H project) and the DFG (Cluster of Excellence UniCat) is gratefully acknowledged. R.S. and P.S. acknowledge funding from the German Federal Ministry of Education and Research (BMBF) under grant 03SF0433A "MEOKATS".

■ REFERENCES

(1) Luo, J.; Im, J.-H.; Mayer, M. T.; Schreier, M.; Nazeeruddin, M. K.; Park, N.-G.; Tilley, S. D.; Fan, H. J.; Gratzel, M. *Science* **2014**, *345*, 1593−1596.

(2) Arico, A. S.; Bruce, P.; Scrosati, B.; Tarascon, J. M.; Van Schalkwijk, W. *Nat. Mater.* **2005**, *4*, 366−377.

(3) Gray, H. B. *Nat. Chem.* **2009**, *1*, 112−112.

(4) Katsounaros, I.; Cherevko, S.; Zeradjanin, A. R.; Mayrhofer, K. J. J. *Angew. Chem., Int. Ed.* **2014**, *53*, 102−121.

DOI: 10.1021/cs501724v
ACS Catal. 2015, 5, 2017−2027

(5) Yuan, C.; Wu, H. B.; Xie, Y.; Lou, X. W. *Angew. Chem., Int. Ed.* **2013**, *53*, 1488−1504.
(6) Meyer, T. J. *Nature* **2008**, *451*, 778−779.
(7) Antolini, E. *Energy Environ. Sci.* **2009**, *2*, 915−931.
(8) Bruce, P. G.; Freunberger, S. A.; Hardwick, L. J.; Tarascon, J. M. *Nat. Mater.* **2011**, *11*, 19−29.
(9) Park, S.; Shao, Y. Y.; Liu, J.; Wang, Y. *Energy Environ. Sci.* **2012**, *5*, 9331−9344.
(10) Winter, M.; Brodd, R. J. *Chem. Rev.* **2004**, *104*, 4245−4269.
(11) Strasser, P.; Koh, S.; Anniyev, T.; Greeley, J.; More, K.; Yu, C.; Liu, Z.; Kaya, S.; Nordlund, D.; Ogasawara, H.; Toney, M. F.; Nilsson, A. *Nat. Chem.* **2010**, *2*, 454−460.
(12) Ferreira, K. N.; Iverson, T. M.; Maghlaoui, K.; Barber, J.; Iwata, S. *Science* **2004**, *303*, 1831−1838.
(13) Dau, H.; Grundmeier, A.; Loja, P.; Haumann, M. *Philos. Trans. R. Soc. B* **2008**, *363*, 1237−1243.
(14) Dau, H.; Limberg, C.; Reier, T.; Risch, M.; Roggan, S.; Strasser, P. *ChemCatChem.* **2010**, *2*, 724−761.
(15) Singh, A.; Spiccia, L. *Coord. Chem. Rev.* **2013**, *257*, 2607−2622.
(16) Wiechen, M.; Najafpour, M. M.; Allakhverdiev, S. I.; Spiccia, L. *Energy Environ. Sci.* **2014**, *7*, 2203−2212.
(17) Oezaslan, M.; Hasche, F.; Strasser, P. *J. Phys. Chem. Lett.* **2013**, *4*, 3273−3291.
(18) Reier, T.; Oezaslan, M.; Strasser, P. *ACS Catal.* **2012**, *2*, 1765−1772.
(19) Lee, Y.; Suntivich, J.; May, K. J.; Perry, E. E.; Shao-Horn, Y. *J. Phys. Chem. Lett.* **2012**, *3*, 399−404.
(20) Neyerlin, K. C.; Bugosh, G.; Forgie, R.; Liu, Z. C.; Strasser, P. *J. Electrochem. Soc.* **2009**, *156*, B363−B369.
(21) Forgie, R.; Bugosh, G.; Neyerlin, K. C.; Liu, Z.; Strasser, P. *Electrochem. Solid State Lett.* **2010**, *13*, D36−D39.
(22) Concepcion, J. J.; Jurss, J. W.; Norris, M. R.; Chen, Z.; Templeton, J. L.; Meyer, T. J. *Inorg. Chem.* **2010**, *49*, 1277−1279.
(23) Duan, L.; Bozoglian, F.; Mandal, S.; Stewart, B.; Privalov, T.; Llobet, A.; Sun, L. *Nat. Chem.* **2012**, *4*, 418−423.
(24) Johnson, B.; Girgsdies, F.; Weinberg, G.; Rosenthal, D.; Knop-Gericke, A.; Schloegl, R.; Reier, T.; Strasser, P. *J. Phys. Chem. C* **2013**, *117*, 25443−25450.
(25) Nong, H. N.; Gan, L.; Willinger, E.; Teschner, D.; Strasser, P. *Chem. Sci.* **2014**, *5*, 2955−2963.
(26) Stoerzinger, K. A.; Qiao, L.; Biegalski, M. D.; Shao-Horn, Y. *J. Phys. Chem. Lett.* **2014**, *5*, 1636−1641.
(27) Antolini, E. *ACS Catal.* **2014**, *4*, 1426−1440.
(28) Cui, C.; Gan, L.; Heggen, M.; Rudi, S.; Strasser, P. *Nat. Mater.* **2013**, *12*, 765−771.
(29) Cui, C.; Gan, L.; Li, H.-H.; Yu, S.-H.; Heggen, M.; Strasser, P. *Nano Lett.* **2012**, *12*, 5885−5889.
(30) Zhang, C.; Hwang, S. Y.; Trout, A.; Peng, Z. *J. Am. Chem. Soc.* **2014**, *136*, 7805−7808.
(31) Chen, Z.; Waje, M.; Li, W.; Yan, Y. *Angew. Chem., Int. Ed.* **2007**, *46*, 4060−4063.
(32) Stamenkovic, V. R.; Fowler, B.; Mun, B. S.; Wang, G.; Ross, P. N.; Lucas, C. A.; Markovic, N. M. *Science* **2007**, *315*, 493−497.
(33) Steele, B. C. H.; Heinzel, A. *Nature* **2001**, *414*, 345−352.
(34) Yang, D.; Li, B.; Zhang, H.; Ma, J. *Int. J. Hydrogen Energy* **2012**, *37*, 2447−2454.
(35) Gasteiger, H. A.; Markovic, N. M. *Science* **2009**, *324*, 48−49.
(36) Huang, S.-Y.; Ganesan, P.; Jung, H.-Y.; Popov, B. N. *J. Power Sources* **2012**, *198*, 23−29.
(37) Nocera, D. G. *Acc. Chem. Res.* **2012**, *45*, 767−776.
(38) Bergmann, A.; Zaharieva, I.; Dau, H.; Strasser, P. *Energy Environ. Sci.* **2013**, *6*, 2745−2755.
(39) Mette, K.; Bergmann, A.; Tessonnier, J.-P.; Haevecker, M.; Yao, L.; Ressler, T.; Schloegl, R.; Strasser, P.; Behrens, M. *ChemCatChem.* **2012**, *4*, 851−862.
(40) Wiechen, M.; Zaharieva, I.; Dau, H.; Kurz, P. *Chem. Sci.* **2012**, *3*, 2330−2339.
(41) Zaharieva, I.; Chernev, P.; Risch, M.; Klingan, K.; Kohlhoff, M.; Fischer, A.; Dau, H. *Energy Environ. Sci.* **2012**, *5*, 7081−7089.
(42) Zaharieva, I.; Najafpour, M. M.; Wiechen, M.; Haumann, M.; Kurz, P.; Dau, H. *Energy Environ. Sci.* **2011**, *4*, 2400−2408.
(43) Robinson, D. M.; Go, Y. B.; Mui, M.; Gardner, G.; Zhang, Z.; Mastrogiovanni, D.; Garfunkel, E.; Li, J.; Greenblatt, M.; Dismukes, G. C. *J. Am. Chem. Soc.* **2013**, *135*, 3494−3501.
(44) Fominykh, K.; Feckl, J. M.; Sicklinger, J.; Doeblinger, M.; Boecklein, S.; Ziegler, J.; Peter, L.; Rathousky, J.; Scheidt, E.-W.; Bein, T.; Fattakhova-Rohlfing, D. *Adv. Funct. Mater.* **2014**, *24*, 3123−3129.
(45) Benbow, E. M.; Kelly, S. P.; Zhao, L.; Reutenauer, J. W.; Suib, S. L. *J. Phys. Chem. C* **2011**, *115*, 22009−22017.
(46) Gorlin, Y.; Jaramillo, T. F. *J. Am. Chem. Soc.* **2010**, *132*, 13612−13614.
(47) Gorlin, Y.; Nordlund, D.; Jaramillo, T. F. *ECS Trans.* **2013**, *58*, 735−750.
(48) Meng, Y.; Song, W.; Huang, H.; Ren, Z.; Chen, S.-Y.; Suib, S. L. *J. Am. Chem. Soc.* **2014**, *136*, 11452−11464.
(49) Liu, Q.; Jin, J.; Zhang, J. *ACS Appl. Mater. Interfaces* **2013**, *5*, 5002−5008.
(50) Cao, X.; Jin, C.; Lu, F.; Yang, Z.; Shen, M.; Yang, R. *J. Electrochem. Soc.* **2014**, *161*, H296−H300.
(51) Gorlin, Y.; Lassalle-Kaiser, B.; Benck, J. D.; Gul, S.; Webb, S. M.; Yachandra, V. K.; Yano, J.; Jaramillo, T. F. *J. Am. Chem. Soc.* **2013**, *135*, 8525−8534.
(52) Wang, D.; Chen, X.; Evans, D. G.; Yang, W. *Nanoscale* **2013**, *5*, 5312−5315.
(53) Cheng, F. Y.; Shen, J. A.; Peng, B.; Pan, Y. D.; Tao, Z. L.; Chen, J. *Nat. Chem.* **2011**, *3*, 79−84.
(54) Sa, J. Y.; Kwon, K.; Cheon, J. Y.; Kleitz, F.; Joo, S. H. *J. Mater. Chem. A* **2013**, *1*, 9992−10001.
(55) Jin, C.; Lu, F.; Cao, X.; Yang, Z.; Yang, R. *J. Mater. Chem. A* **2013**, *1*, 12170−12177.
(56) Zhao, A.; Masa, J.; Xia, W.; Maljusch, A.; Willinger, M.-G.; Clavel, G.; Xie, K.; Schloegl, R.; Schuhmann, W.; Muhler, M. *J. Am. Chem. Soc.* **2014**, *136*, 7551−7554.
(57) Maiyalagan, T.; Jarvis, K. A.; Therese, S.; Ferreira, P. J.; Manthiram, A. *Nat. Commun.* 2014, *5*.
(58) Grimaud, A.; Carlton, C. E.; Risch, M.; Hong, W. T.; May, K. J.; Shao-Horn, Y. *J. Phys. Chem. C* **2013**, *117*, 25926−25932.
(59) May, K. J.; Carlton, C. E.; Stoerzinger, K. A.; Risch, M.; Suntivich, J.; Lee, Y.-L.; Grimaud, A.; Shao-Horn, Y. *J. Phys. Chem. Lett.* **2012**, *3*, 3264−3270.
(60) Suntivich, J.; May, K. J.; Gasteiger, H. A.; Goodenough, J. B.; Shao-Horn, Y. *Science* **2012**, *334*, 1383−1385.
(61) Suntivich, J.; Perry, E. E.; Gasteiger, H. A.; Shao-Horn, Y. *Electrocatal.* **2013**, *4*, 49−55.
(62) Suntivich, J.; Shao-Horn, Y. *ECS Trans.* **2013**, *58*, 715−26.
(63) Risch, M.; Stoerzinger, K. A.; Maruyama, S.; Hong, W. T.; Takeuchi, I.; Shao-Horn, Y. *J. Am. Chem. Soc.* **2014**, *136*, 5229−5232.
(64) Liang, Y.; Li, Y.; Wang, H.; Zhou, J.; Wang, J.; Regier, T.; Dai, H. *Nat. Mater.* **2011**, *10*, 780−786.
(65) Mao, S.; Wen, Z. H.; Huang, T. Z.; Hou, Y.; Chen, J. H. *Energy Environ. Sci.* **2014**, *7*, 609−616.
(66) Weiyong, B.; Zhenrong, Y.; Strasser, P.; Ruizhi, Y. *J. Power Sources* **2014**, *250*, 196−203.
(67) McKone, J. R.; Lewis, N. S.; Gray, H. B. *Chem. Mater.* **2013**, *26*, 407−414.
(68) Indra, A.; Menezes, P. W.; Schwarze, M.; Driess, M. *N. J. Chem.* **2014**, *38*, 1942−1945.
(69) (a) Indra, A.; Menezes, P. W.; Zaharieva, I.; Baktash, E.; Pfrommer, J.; Schwarze, M.; Dau, H.; Driess, M. *Angew. Chem., Int. Ed.* **2013**, *52*, 13206−13210. (b) Indra, A.; Menezes, P. W.; Driess, M. *ChemSusChem* **2015**, DOI: 10.1002/cssc.201402812.
(70) Menezes, P. W.; Indra, A.; Littlewood, P.; Schwarze, M.; Goebel, C.; Schomaecker, R.; Driess, M. *ChemSusChem* **2014**, *7*, 2202−2211.
(71) Pfrommer, J.; Lublow, M.; Azarpira, A.; Gobel, C.; Lucke, M.; Steigert, A.; Pogrzeba, M.; Menezes, P. W.; Fischer, A.; Schedel-Niedrig, T.; Driess, M. *Angew. Chem., Int. Ed.* **2014**, *53*, 5183−5187.

DOI: 10.1021/cs501724v
ACS Catal. 2015, 5, 2017−2027

(72) Indra, A.; Menezes, P. W.; Sahraie, N. R.; Bergmann, A.; Das, C.; Tallarida, M.; Schmeisser, D.; Strasser, P.; Driess, M. *J. Am. Chem. Soc.* **2014**, *136*, 17530−17536.
(73) Menezes, P. W.; Indra, A.; Sahraie, N. R.; Bergmann, A.; Strasser, P.; Driess, M. *ChemSusChem* **2015**, *8*, 164−171.
(74) Aksu, Y.; Driess, M. *Angew. Chem., Int. Ed.* **2009**, *48*, 7778−7782.
(75) Aksu, Y.; Frasca, S.; Wollenberger, U.; Driess, M.; Thomas, A. *Chem. Mater.* **2011**, *23*, 1798−1804.
(76) Heitz, S.; Aksu, Y.; Merschjann, C.; Driess, M. *Chem. Mater.* **2010**, *22*, 1376−1385.
(77) Heitz, S.; Epping, J.-D.; Aksu, Y.; Driess, M. *Chem. Mater.* **2010**, *22*, 4563−4571.
(78) Polarz, S.; Orlov, A. V.; van den Berg, M. W. E.; Driess, M. *Angew. Chem., Int. Ed.* **2005**, *44*, 7892−7896.
(79) Samedov, K.; Aksu, Y.; Driess, M. *Chem. Mater.* **2012**, *24*, 2078−2090.
(80) Roth, W. L. *J. Phys. Chem. Solids* **1964**, *25*, 1−10.
(81) Oku, M.; Hirokawa, K. *J. Electron Spectrosc. Relat. Phenom.* **1976**, *8*, 475−481.
(82) Kent, C. A.; Concepcion, J. J.; Dares, C. J.; Torelli, D. A.; Rieth, A. J.; Miller, A. S.; Hoertz, P. G.; Meyer, T. J. *J. Am. Chem. Soc.* **2013**, *135*, 8432−8435.
(83) Yuan, X.; Zhang, M.; Chen, X.; An, N.; Liu, G.; Liu, Y.; Zhang, W.; Yan, W.; Jia, M. *Appl. Catal., A* **2012**, *439*, 149−155.
(84) Shinde, V.; Mandale, A. B.; Patil, K. R.; Gaikwad, A. B.; Patil, P. P. *Surf. Coat. Technol.* **2006**, *200*, 5094−5101.
(85) Song, W.; Poyraz, A. S.; Meng, Y.; Ren, Z.; Chen, S.-Y.; Suib, S. L. *Chem. Mater.* **2014**, *26*, 4629−4639.
(86) Tan, B. J.; Klabunde, K. J.; Sherwood, P. M. A. *J. Am. Chem. Soc.* **1991**, *113*, 855−861.
(87) Ma, S.; Sun, L.; Cong, L.; Gao, X.; Yao, C.; Guo, X.; Tai, L.; Mei, P.; Zeng, Y.; Xie, H.; Wang, R. *J. Phys. Chem. C* **2013**, *117*, 25890−25897.
(88) Li, J.; Wang, J.; Liang, X.; Zhang, Z.; Liu, H.; Qian, Y.; Xiong, S. *ACS Appl. Mater. Interfaces* **2014**, *6*, 24−30.
(89) Kanan, M. W.; Nocera, D. G. *Science* **2008**, *321*, 1072−1075.
(90) Lutterman, D. A.; Surendranath, Y.; Nocera, D. G. *J. Am. Chem. Soc.* **2009**, *131*, 3838−3839.
(91) Surendranath, Y.; Kanan, M. W.; Nocera, D. G. *J. Am. Chem. Soc.* **2010**, *132*, 16501−16509.
(92) Singh, R. N.; Mishra, D.; Anindita; Sinha, A. S. K.; Singh, A. *Electrochemi. Commun.* **2007**, *9*, 1369−1373.
(93) Esswein, A. J.; McMurdo, M. J.; Ross, P. N.; Bell, A. T.; Tilley, T. D. *J. Phys. Chem. C* **2009**, *113*, 15068−15072.
(94) Blakemore, J. D.; Gray, H. B.; Winkler, J. R.; Mueller, A. M. *ACS Catal.* **2013**, *3*, 2497−2500.
(95) Blakemore, J. D.; Schley, N. D.; Olack, G. W.; Incarvito, C. D.; Brudvig, G. W.; Crabtree, R. H. *Chem. Sci.* **2011**, *2*, 94−98.
(96) Grzelczak, M.; Zhang, J. S.; Pfrommer, J.; Hartmann, J.; Driess, M.; Antonietti, M.; Wang, X. C. *ACS Catal.* **2013**, *3*, 383−388.
(97) Koza, J. A.; He, Z.; Miller, A. S.; Switzer, J. A. *Chem. Mater.* **2012**, *24*, 3567−3573.
(98) Nam Hawn, C.; Ross, P. N.; Bell, A. T.; Tilley, T. D. *ChemSusChem* **2011**, *4*, 1566−1569.
(99) Zhuang, Z. B.; Sheng, W. C.; Yan, Y. S. *Adv. Mater.* **2014**, *26*, 3950−3955.
(100) Liu, X.; Chang, Z.; Luo, L.; Xu, T.; Lei, X.; Liu, J.; Sun, X. *Chem. Mater.* **2014**, *26*, 1889−1895.
(101) Deng, X.; Tuysuz, H. *ACS Catal.* **2014**, *4*, 3701−3714.
(102) McCrory, C. C. L.; Jung, S.; Peters, J. C.; Jaramillo, T. F. *J. Am. Chem. Soc.* **2014**, *135*, 16977−16987.
(103) Gorlin, Y.; Chung, C.-J.; Benck, J. D.; Nordlund, D.; Seitz, L.; Weng, T.-C.; Sokaras, D.; Clemens, B. M.; Jaramillo, T. F. *J. Am. Chem. Soc.* **2014**, *136*, 4920−4926.
(104) Wang, Y.; Zhou, T.; Jiang, K.; Da, P.; Peng, Z.; Tong, J.; Kong, B.; Cai, W.-B.; Yang, Y.; Zheng, G. *Adv. Energy Mater.* **2014**, DOI: 10.1002/aenm.201470082.
(105) Gao, M.; Sheng, W.; Zhuang, Z.; Fang, Q.; Gu, S.; Jiang, J.; Yan, Y. *J. Am. Chem. Soc.* **2014**, *136*, 7077−7084.
(106) Kim, T. W.; Woo, M. A.; Regis, M.; Choi, K.-S. *J. Phys. Chem. Lett.* **2014**, *5*, 2370−2374.
(107) Klingan, K.; Ringleb, F.; Zaharieva, I.; Heidkamp, J.; Chernev, P.; Gonzalez-Flores, D.; Risch, M.; Fischer, A.; Dau, H. *ChemSusChem* **2014**, *7*, 1301−1310.
(108) Cherevko, S.; Zeradjanin, A. R.; Topalov, A. A.; Kulyk, N.; Katsounaros, I.; Mayrhofer, K. J. J. *ChemCatChem.* **2014**, *6*, 2219−2223.
(109) Lee, S. W.; Carlton, C.; Risch, M.; Surendranath, Y.; Chen, S.; Furutsuki, S.; Yamada, A.; Nocera, D. G.; Shao-Horn, Y. *J. Am. Chem. Soc.* **2012**, *134*, 16959−16962.
(110) Young, E. R.; Nocera, D. G.; Bulovic, V. *Energy Environ. Sci.* **2010**, *3*, 1726−1728.
(111) Jiao, F.; Frei, H. *Angew. Chem., Int. Ed.* **2009**, *48*, 1841−1844.
(112) Jiao, F.; Frei, H. *Chem. Commun.* **2010**, *46*, 2920−2922.
(113) Jiao, F.; Frei, H. *Energy Environ. Sci.* **2010**, *3*, 1018−1027.
(114) Yusuf, S.; Jiao, F. *ACS Catal.* **2012**, *2*, 2753−2760.
(115) Rosen, J.; Hutchings, G. S.; Jiao, F. *J. Am. Chem. Soc.* **2013**, *135*, 4516−4521.
(116) Hong, D.; Yamada, Y.; Nomura, A.; Fukuzumi, S. *Phys. Chem. Chem. Phys.* **2013**, *15*, 19125−19128.
(117) Hong, D.; Yamada, Y.; Nagatomi, T.; Takai, Y.; Fukuzumi, S. *J. Am. Chem. Soc.* **2012**, *134*, 19572−19575.
(118) Zhang, Y.; Rosen, J.; Hutchings, G. S.; Jiao, F. *Catal. Today* **2914**, *225*, 171−176.
(119) Rosen, J.; Hutchings, G. S.; Jiao, F. *J. Catal.* **2014**, *310*, 2−9.
(120) Liang, Y.; Li, Y.; Wang, H.; Dai, H. *J. Am. Chem. Soc.* **2013**, *135*, 2013−2036.
(121) Lambert, T. N.; Davis, D. J.; Lu, W.; Limmer, S. J.; Kotula, P. G.; Thuli, A.; Hungate, M.; Ruan, G.; Jin, Z.; Tour, J. M. *Chem. Commun.* **2012**, *48*, 7931−7933.
(122) Du, J.; Pan, Y.; Zhang, T.; Han, X.; Cheng, F.; Chen, J. *J. Mater. Chem.* **2012**, *22*, 15812−15818.
(123) Xiao, J.; Kuang, Q.; Yang, S.; Xiao, F.; Wang, S.; Guo, L. *Sci. Rep.* **2013**, *3*, 2300.
(124) Masa, J.; Xia, W.; Sinev, I.; Zhao, A.; Sun, Z.; Gruetzke, S.; Weide, P.; Muhler, M.; Schuhmann, W. *Angew. Chem., Int. Ed.* **2014**, *53*, 8508−8512.
(125) Liang, Y.; Wang, H.; Zhou, J.; Li, Y.; Wang, J.; Regier, T.; Dai, H. *J. Am. Chem. Soc.* **2012**, *134*, 3517−3523.
(126) Roche, I.; Chainet, E.; Chatenet, M.; Vondrak, J. *J. Phys. Chem. C* **2007**, *111*, 1434−1443.
(127) Roche, I.; Chainet, E.; Vondrak, J.; Chatenet, M. *J. Appl. Electrochem.* **2008**, *38*, 1195−1201.
(128) Spencer, C. D.; Schroeer, D. *Phys. Rev. B* **1974**, *9*, 3658−3665.
(129) Beaufils, J. P.; Barbaux, Y. *J. Appl. Crystallogr.* **1982**, *15*, 301−7.
(130) Ziolkowski, J.; Barbaux, Y. *J. Mol. Catal.* **1991**, *67*, 199−215.
(131) Rios, E.; Chartier, P.; Gautier, J. L. *Solid State Sci.* **1999**, *1*, 267−277.
(132) Rios, E.; Reyes, H.; Ortiz, J.; Gautier, J. L. *Electrochim. Acta* **2005**, *50*, 2705−2711.
(133) Hamdani, M.; Singh, R. N.; Chartier, P. *Int. J. Electrochem. Sci.* **2010**, *5*, 556−577.
(134) Xie, X.; Li, Y.; Liu, Z.-Q.; Haruta, M.; Shen, W. *Nature* **2009**, *458*, 746−749.
(135) Sun, Y.; Lv, P.; Yang, J.-Y.; He, L.; Nie, J.-C.; Liu, X.; Li, Y. *Chem. Commun.* **2011**, *47*, 11279−11281.
(136) Jiao, F.; Frei, H. *Chem. Commun.* **2012**, *46*, 2920−2922.

DOI: 10.1021/cs501724v
ACS Catal. 2015, 5, 2017−2027